SUPPLEMENTARY INFORMATION

Intrinsic aging in mixed-cation lead halide perovskites

Fernando B. Minussi[1*], Eduardo M. Bertoletti[1], José A. Eiras[2], Eudes B. Araújo[1]

[1] Department of Physics and Chemistry, São Paulo State University, 15385-000 Ilha Solteira, Brazil

[2] Department of Physics, Federal University of São Carlos, 13565-905 São Carlos, Brazil

Supplementary Note 1: Surface segregates in aged $MAPbI_3$

[*] corresponding author: fbminussi@gmail.com

When analyzed through scanning electron microscopy, PbI_2 crystals are expected to look brighter than perovskite crystals due to the higher average atomic number [1]. Small surface, bright segregated were not present in pristine $MAPbI_3$ and began to be identified in the microstructure of aged samples as shown in Fig. S1, which are likely to be PbI_2. Note that the quantity of such segregates increases with the aging time, consistent with progressive surface degradation phenomena. After three months, these particles were more concentrated near grain boundaries and/or small grains, whereas they were spread over the entire surface after six months. More images for better comparison are given in Supplementary Note 6.

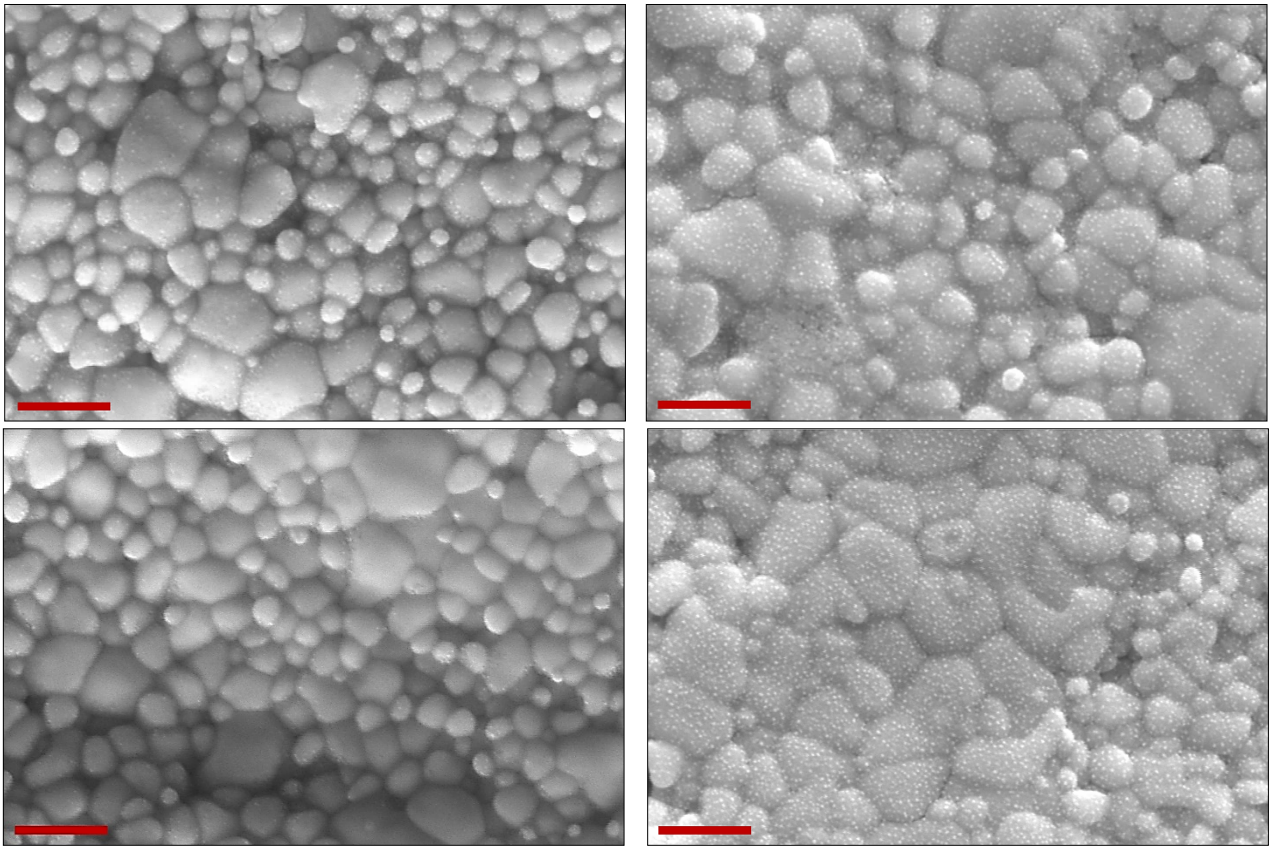

Fig. S1 - SEM images of 3 months (left) and 6 months-aged (right) polycrystalline $MAPbI_3$ samples. Scale bars: 2 μm.

Supplementary Note 2: The possible precipitation of $GAPbI_3$ in $GA_xMA_{1-x}PbI_3$

As discussed in the ESI file of recent work [2], elongated crystals, attributed to $GAPbI_3$ segregates, are commonly present in the microstructure of $GA_xMA_{1-x}PbI_3$ pellets for GA^+ contents above the solubility limit. In our samples, these elongated crystals were present in pristine samples of $x = 0.3$ and $x = 0.4$ compositions (Supplementary Note 3) but not for x up to 0.2 compositions (Supplementary Note 6). However, such elongated crystals started to be noticed in 3 months-aged $GA_{0.1}MA_{0.9}PbI_3$ and $GA_{0.2}MA_{0.8}PbI_3$ samples, as shown in Fig. S2. Due to the morphological similarity, we believe that these crystals might be of $GAPbI_3$ segregates as well. This would imply that a phase separation phenomenon occurs even when the compositions are below the experimentally verified solubility limit of GA^+ in the $MAPbI_3$ host matrix.

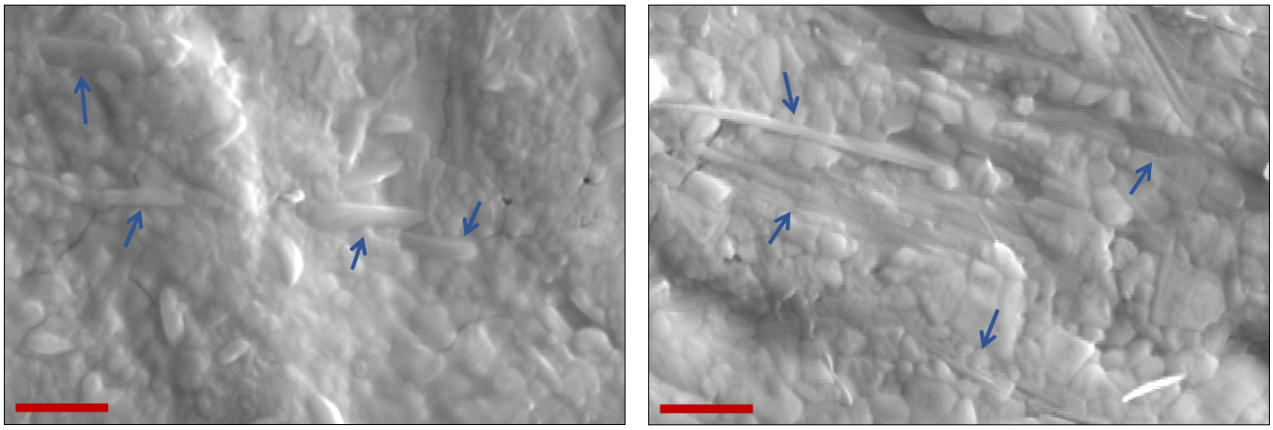

Fig. S2 - SEM images of 3 months-aged polycrystalline $GA_{0.1}MA_{0.9}PbI_3$ (left) and $GA_{0.2}MA_{0.8}PbI_3$ (right) samples. Arrows indicate possible $GAPbI_3$ segregates. Scale bars: 2 μm.

Important to mention that this alledged $GAPbI_3$ segregation is possibly a surface-localized phenomenon, at least for the $x = 0.1$ composition. We speculate it because there is no indication of such a phase in its diffractograms. Thus, the fraction of a second phase should be quite small. Eventually, the bulk constraints can increase activation energies for this segregation, preventing it from occurring anywhere but on the surface. Noteworthy, the supposed segregates of $GAPbI_3$ are not found on the entire surface. On the contrary, they are constituents that appear in a few parts of the samples.

Supplementary Note 3: The possible progressive $GAPbI_3$ precipitation in $GA_xMA_{1-x}PbI_3$

To test the hypothesis of a progressive $GAPbI_3$ segregation over time, we characterized two $GA_xMA_{1-x}PbI_3$ compositions above the solubility limit, namely $GA_{0.3}MA_{0.7}PbI_3$ (x = 0.3) and $GA_{0.4}MA_{0.6}PbI_3$ (x = 0.4). The results are shown in Fig. S3. As observed in Fig. S3a, the typical elongated structures associated with $GAPbI_3$ crystals were already present in the pristine samples. These samples were aged following the same procedure described in the main text, and the respective X-ray diffractograms were collected over time (Fig. S3b).

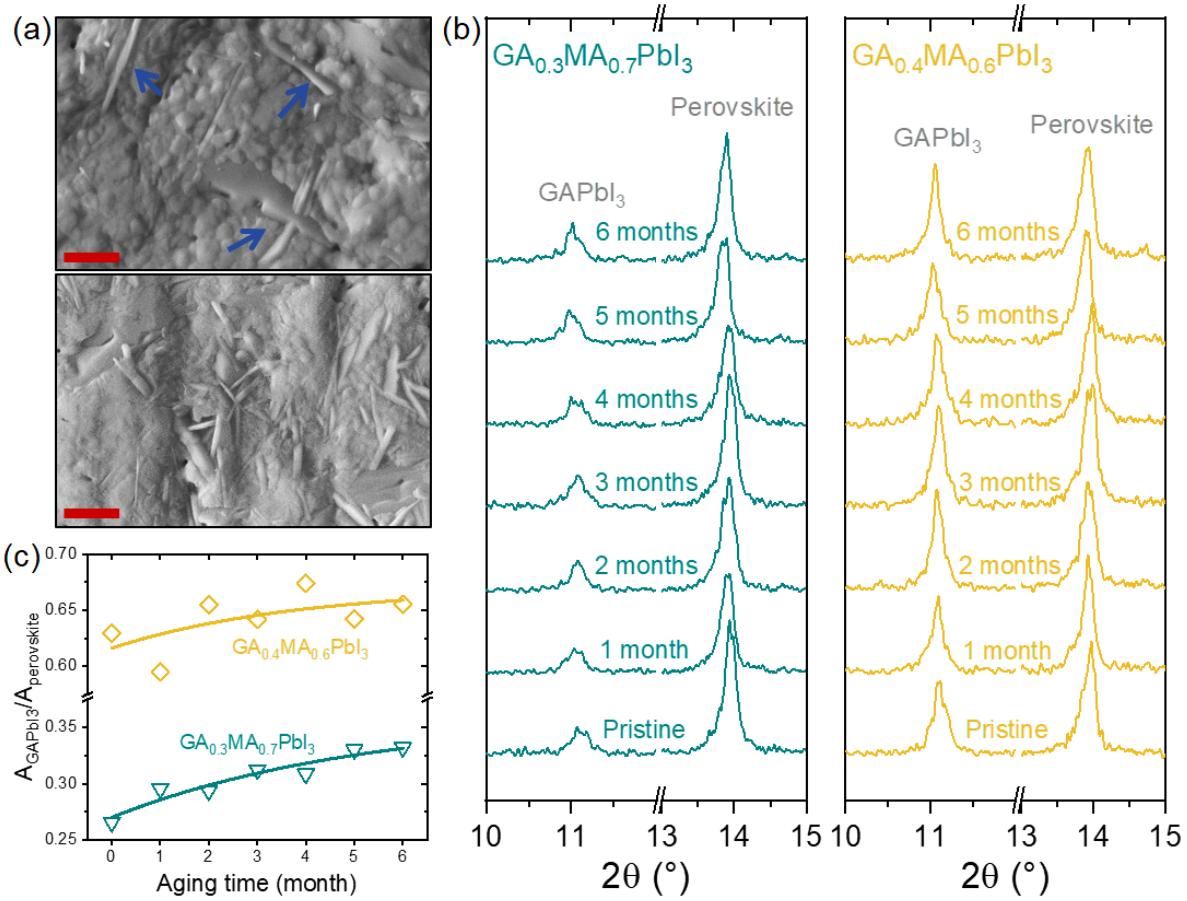

Fig. S3 - (a) SEM images of pristine $GA_{0.3}MA_{0.7}PbI_3$ (top) and $GA_{0.4}MA_{0.6}PbI_3$ (bottom) samples. Arrows indicate $GAPbI_3$ segregates in $GA_{0.3}MA_{0.7}PbI_3$, which are abundant in $GA_{0.4}MA_{0.6}PbI_3$. Scale bars: 2 μm. (b) XRD profiles as a function of aging time on selected 2θ intervals, showing only the main $GAPbI_3$ and perovskite peaks. (c) Aging dependence of XRD $GAPbI_3$/perovskite peaks area ratios. Lines are guides to the eyes.

Considering $GAPbI_3$ and perovskite phase prominent peaks, we searched for a possible evolution of the proportion between these phases by comparing the areas of respective peaks. The results are shown in Fig. S3c. As can be seen, there is a clear tendency for both compositions to increase the are the ratio between the peaks, which is possibly a consequence of the progressive segregation of $GAPbI_3$. Let's consider that the matrix of these compositions is initially saturated in GA^+, with the composition predicted by the solubility limit (as would be expected under

thermodynamic equilibrium). The segregation of $GAPbI_3$ with time causes the reduction of the GA^+ concentration in the matrix to below the solubility limit. In principle, this means that the segregation of $GAPbI_3$ occurs even in the unsaturated solid solution matrix, as speculated in the main text discussion. We speculate that $GA_xMA_{1-x}PbI_3$ compositions might form metastable solid solutions based on that discussion.

Supplementary Note 4: Le Bail fits of X-ray diffraction data

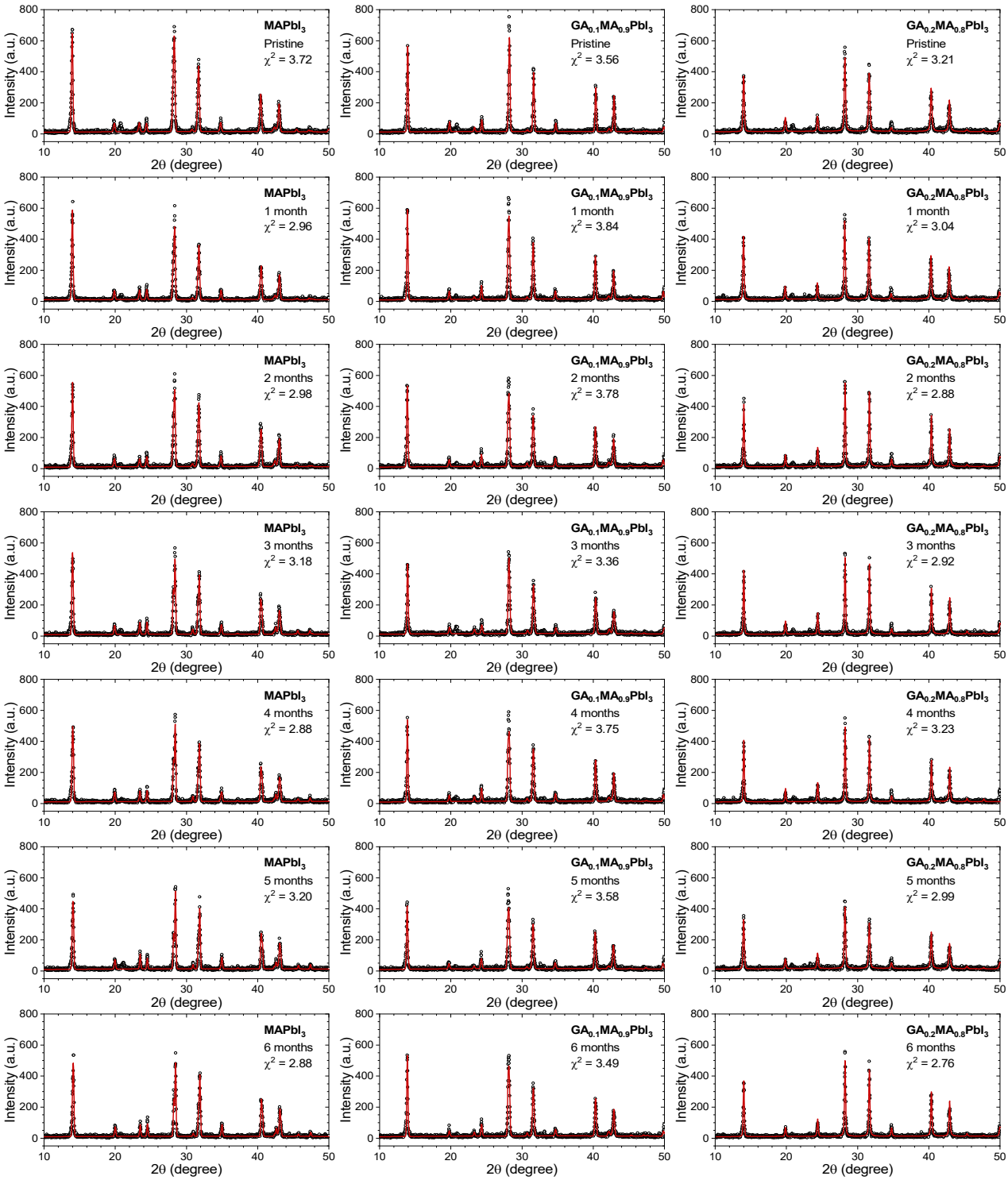

Fig. S4 - Experimental (black circles) and calculated (red lines) XRD data used to calculate lattice parameters of the $GA_xMA_{1-x}PbI_3$ compositions as a function of aging. Le Bail fits of XRD data were obtained using WinPLOTR implemented in the FullProf software [3] (march 2021 version). The χ^2 values were given by the FullProf software.

Supplementary Note 5: Chemical composition evolution with aging

In Fig. S5, we show the variation of the I/Pb molar ratio of our $GA_xMA_{1-x}PbI_3$ samples with aging time. The changes are much more intense for the pure $MAPbI_3$ than for the others. From 0 to 3 months, the I/Pb molar ratio is reduced by about 7%. Note that only in $MAPbI_3$ are there changes out of the error ranges of the EDX technique. For this reason, we believe it is plausible that the iodine loss is considerably greater in this composition than in those containing guanidinium. In the main text, we hypothesized the formation of small amounts of PbI_2 located at the surface, which, among other factors, might derive from the idea that surface reactions would have lower activation energies. We proposed that reducing the I/Pb molar ratio is a possible consequence of iodine-containing molecule release. The induced PbI_2 formation by a reducing I/Pb ratio is corroborated elsewhere [4]. Hence, although we do not exclude the possibility of non-halogenated organic molecules losses, such as CH_3NH_2, we argue that the release of iodine-based molecules, including molecular iodine, is also possible.

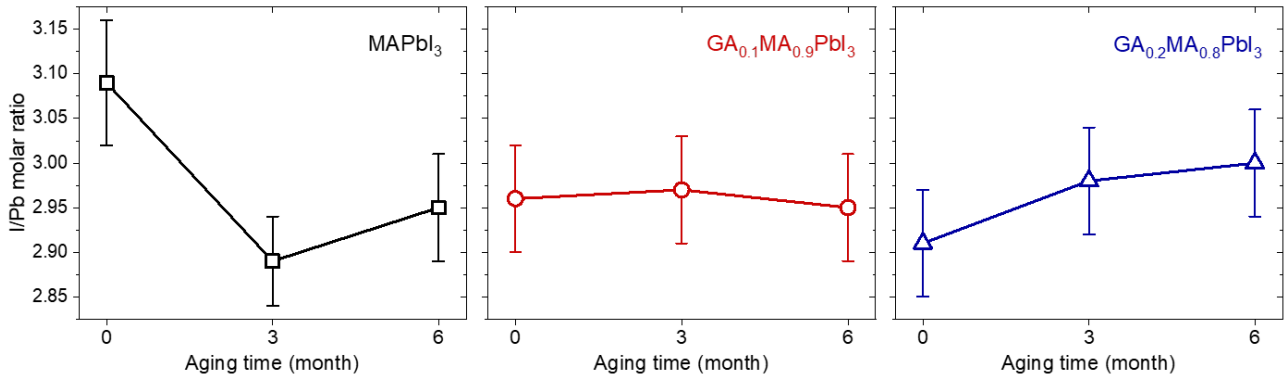

Fig. S5 - Iodine/lead molar ratio for the $GA_xMA_{1-x}PbI_3$ compositions as a function of aging time. Estimations based on EDX analyses of 500x magnified regions. Error bars were calculated from the measurement uncertainties of the technique.

Supplementary Note 6: Microstructural aging evolution

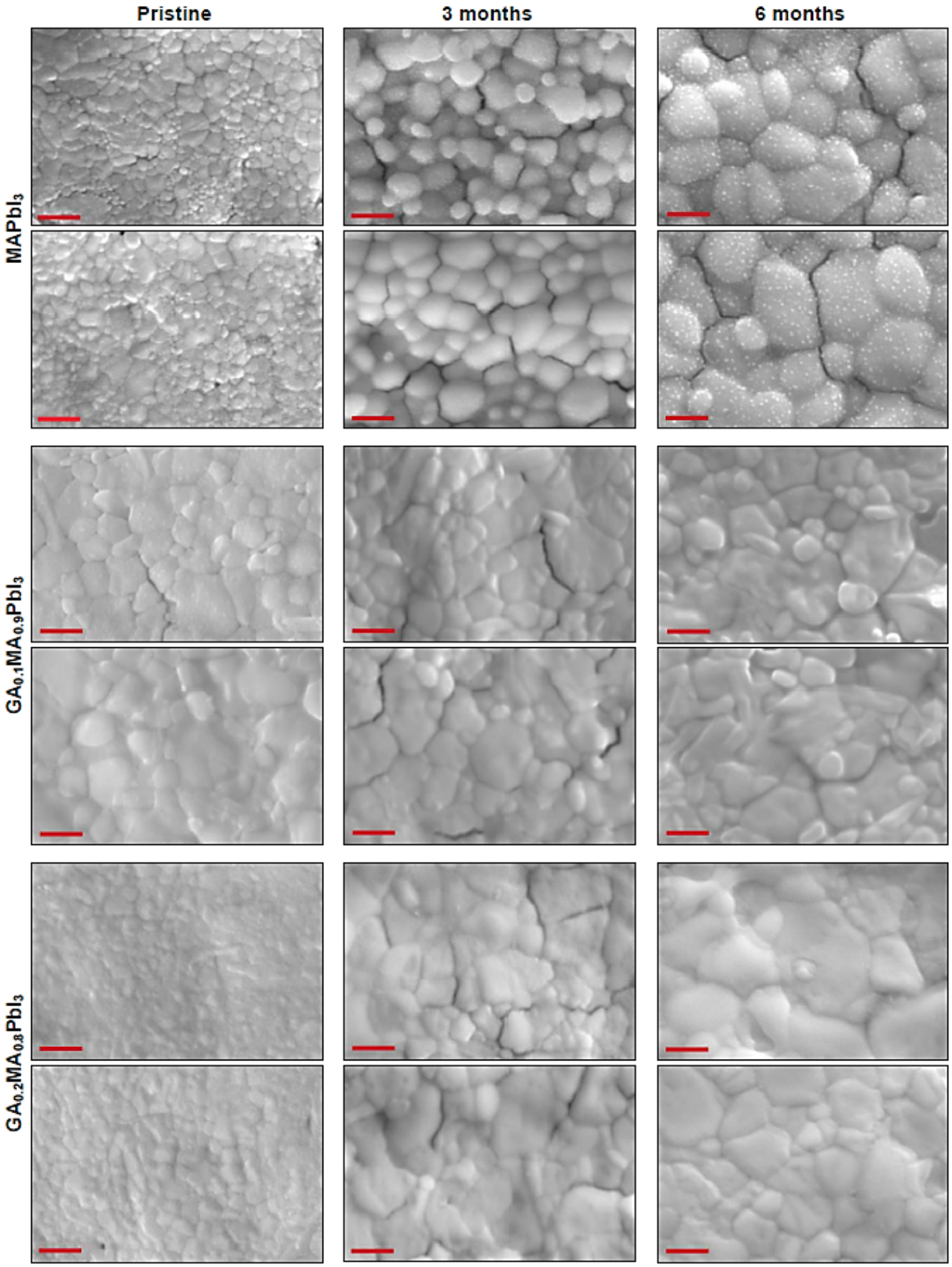

Fig. S6 - Microstructural evolution of $GA_xMA_{1-x}PbI_3$ pellets with aging. Scale bars: 1 μm.

Supplementary Note 7: Abnormal grain growth in $MAPbI_3$

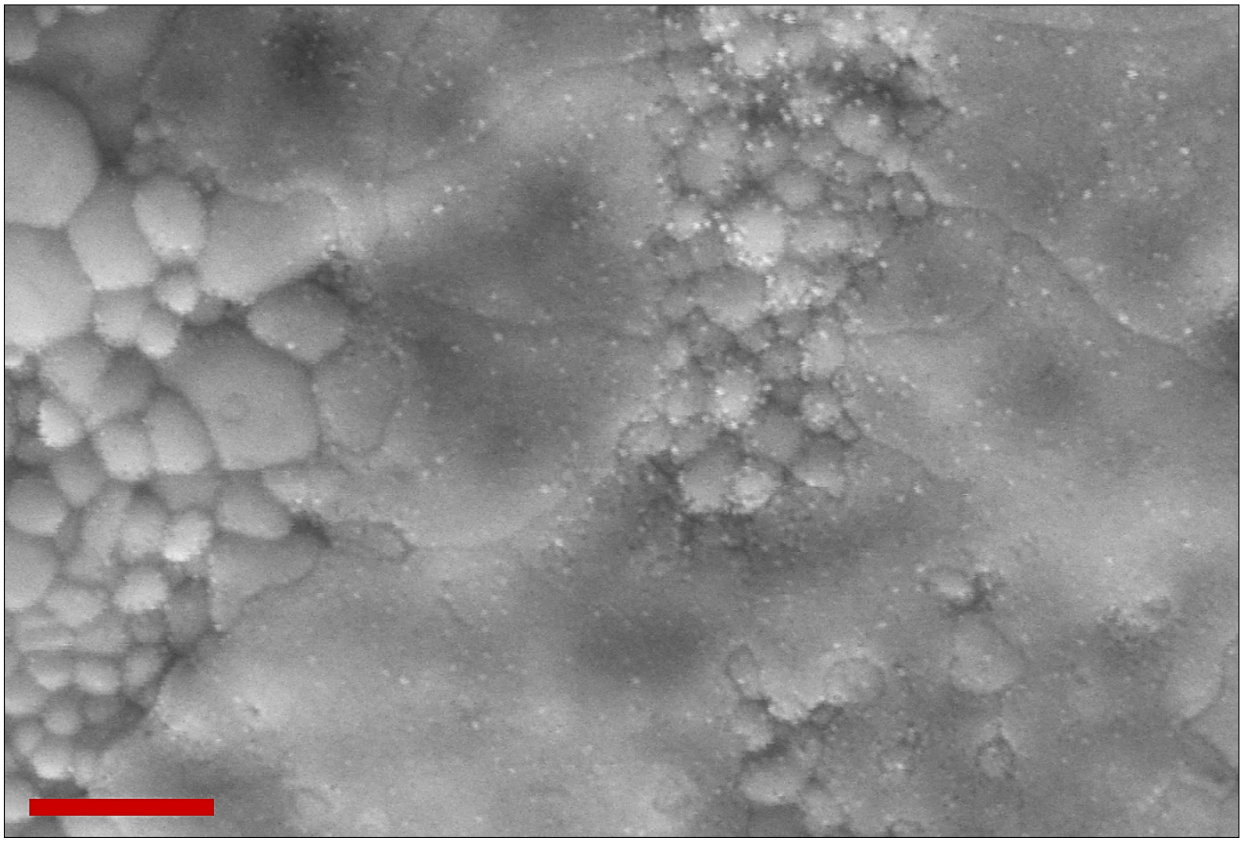

Fig. S7 - SEM image of 3 months-aged $MAPbI_3$ showing abnormally large grains. Scale bars: 2 μm.

Supplementary Note 8: Aging-dependency of the band gap energies

For each $GA_xMA_{1-x}PbI_3$ composition during the aging, we set up the respective Tauc plots from UV/Vis diffuse reflectance data, shown in Fig. S8. The band gap energies (E_g) were calculated using the Tauc equation, given by $(\alpha h\nu)^{1/\gamma} = B(h\nu - E_g)$ where α is the extinction coefficient, h is the Planck constant, ν is the photon's frequency, γ is a factor that depends on the nature of the electron transition, and B is a constant. In our analysis, we considered electronic transitions related to a direct band gap (γ = 1/2), which is often reported for halide perovskites [5].

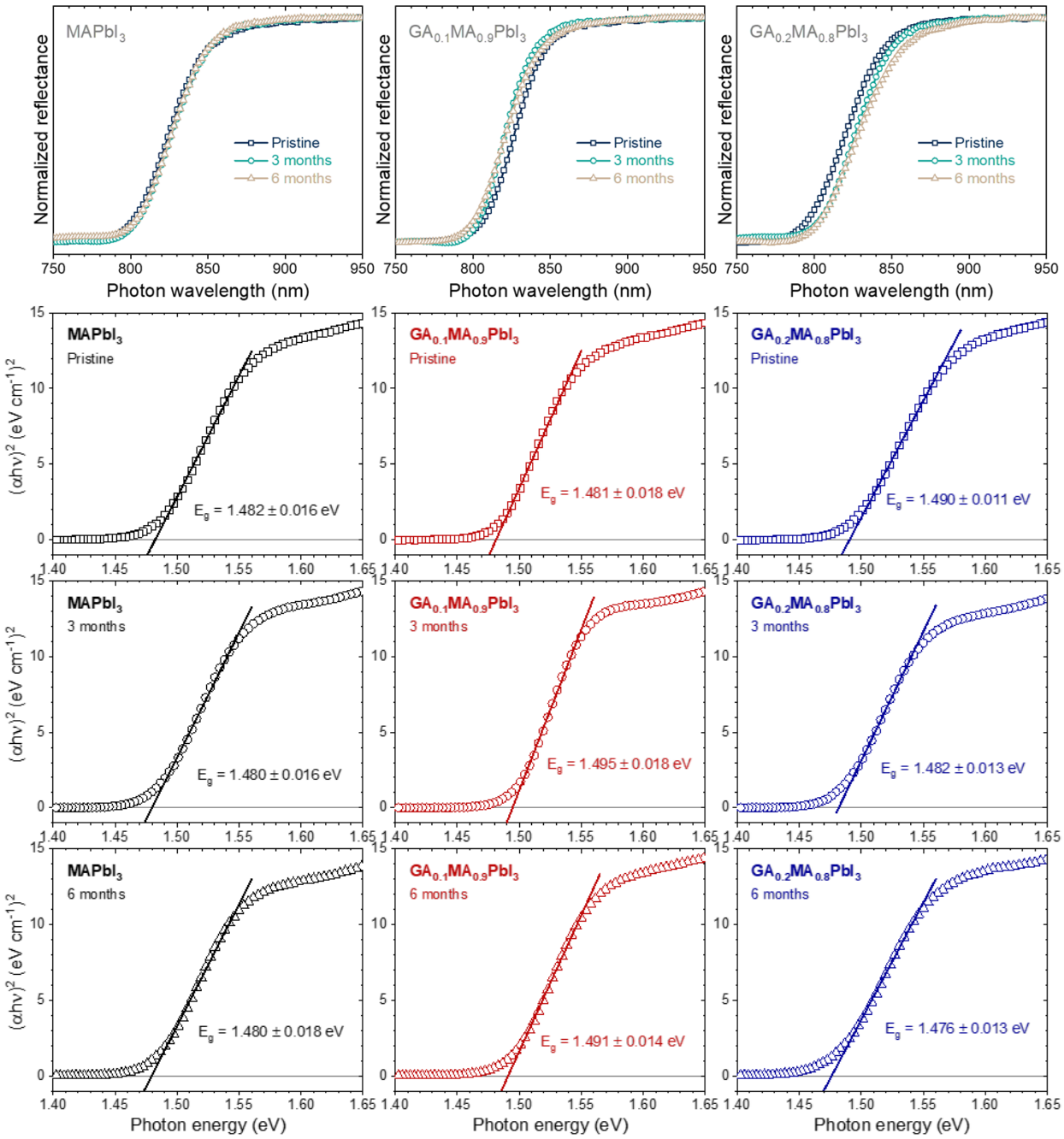

Fig. S8 - Aging evolution of normalized UV/Vis diffuse reflectance (top) and Tauc plots (bottom), showing the respective band gap energies, of $GA_xMA_{1-x}PbI_3$ pellets. Thick lines are the fits to the Tauc equation.

Supplementary Note 9: Aging evolution of the J-V hysteresis

To evaluate the J-V hysteresis, we measured the current-voltage (I-V) curves for up-and-down electric potentials using a 0.1 V m^{-1} scan rate. The difference between measured currents was plotted against the potential for each composition, and the resulting curves were integrated. Since the $GA_xMA_{1-x}PbI_3$ pellets had different thicknesses (650, 480, and 550 μm for x = 0.0, 0.1, and 0.2, respectively), we normalized the values to the geometric parameters of each sample by dividing the obtained areas by the product of the electrode area (3.47 x 10^{-7} m^2) and the sample thicknesses. The resulting values have dimensions of energy per volume per time unit. The estimated J-V hysteresis for each composition/aging time was the mean of results from I-V data collected on three electrodes across the sample. The experimental curves are shown in Figs. S9 to S11. The respective results are given in Table S1. In Fig. S12 is shown the effect of aging on the J-V hysteresis for x = 0.2. Due to the possible $GAPbI_3$ segregation over time in this composition, a trend with aging is not clearly seen.

Table S1 - Results of the J-V hysteresis for the $GA_xMA_{1-x}PbI_3$ compositions on each aging time. The uncertainties are the standard deviations.

Composition	**J-V hysteresis (W m^{-3})**						
	Pristine	**1 month**	**2 months**	**3 months**	**4 months**	**5 months**	**6 months**
x = 0.0	699	190	407	466	214	188	186
	572	82	453	448	260	309	54
	952	76	363	227	200	11	38
	741 ± 190	116 ± 64	408 ± 45	380 ± 130	224 ± 31	169 ± 150	93 ± 81
x = 0.1	294	56	62	95	113	80	57
	595	66	126	172	88	74	53
	435	39	150	151	69	82	54
	441 ± 150	54 ± 14	113 ± 45	139 ± 40	90 ± 22	79 ± 4	55 ± 2
x = 0.2	82	32	799	1078	32	34	69
	54	18	361	927	38	16	163
	93	14	243	231	48	16	324
	76 ± 20	21 ± 10	467 ± 290	745 ± 450	39 ± 8	22 ± 11	185 ± 130

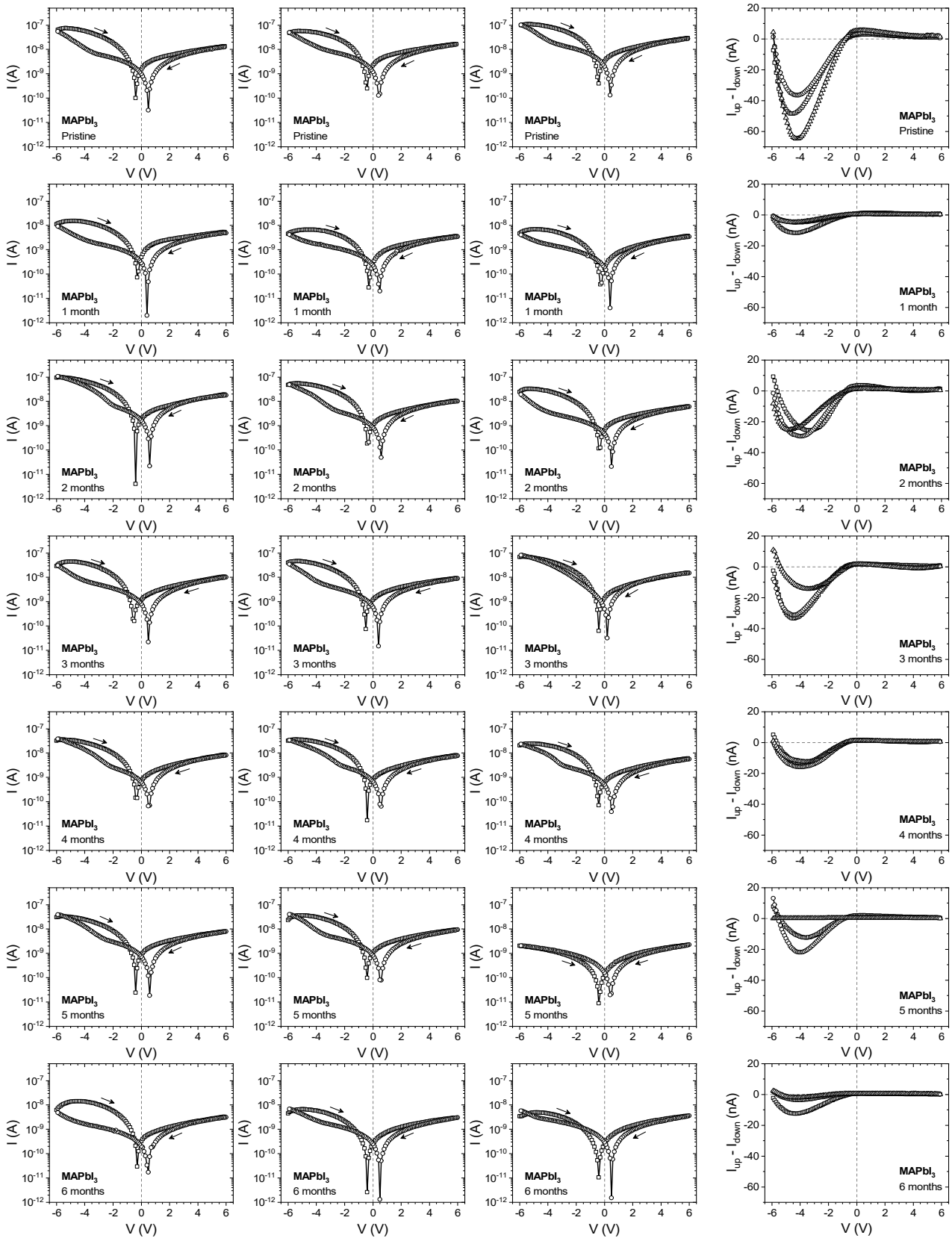

Fig. S9 - Aging evolution of up/down current-voltage curves for $MAPbI_3$ on three electrodes. Arrows indicate the direction of measurement. Graphs to the right are the differences between up and down curves at each electrode for a given aging time.

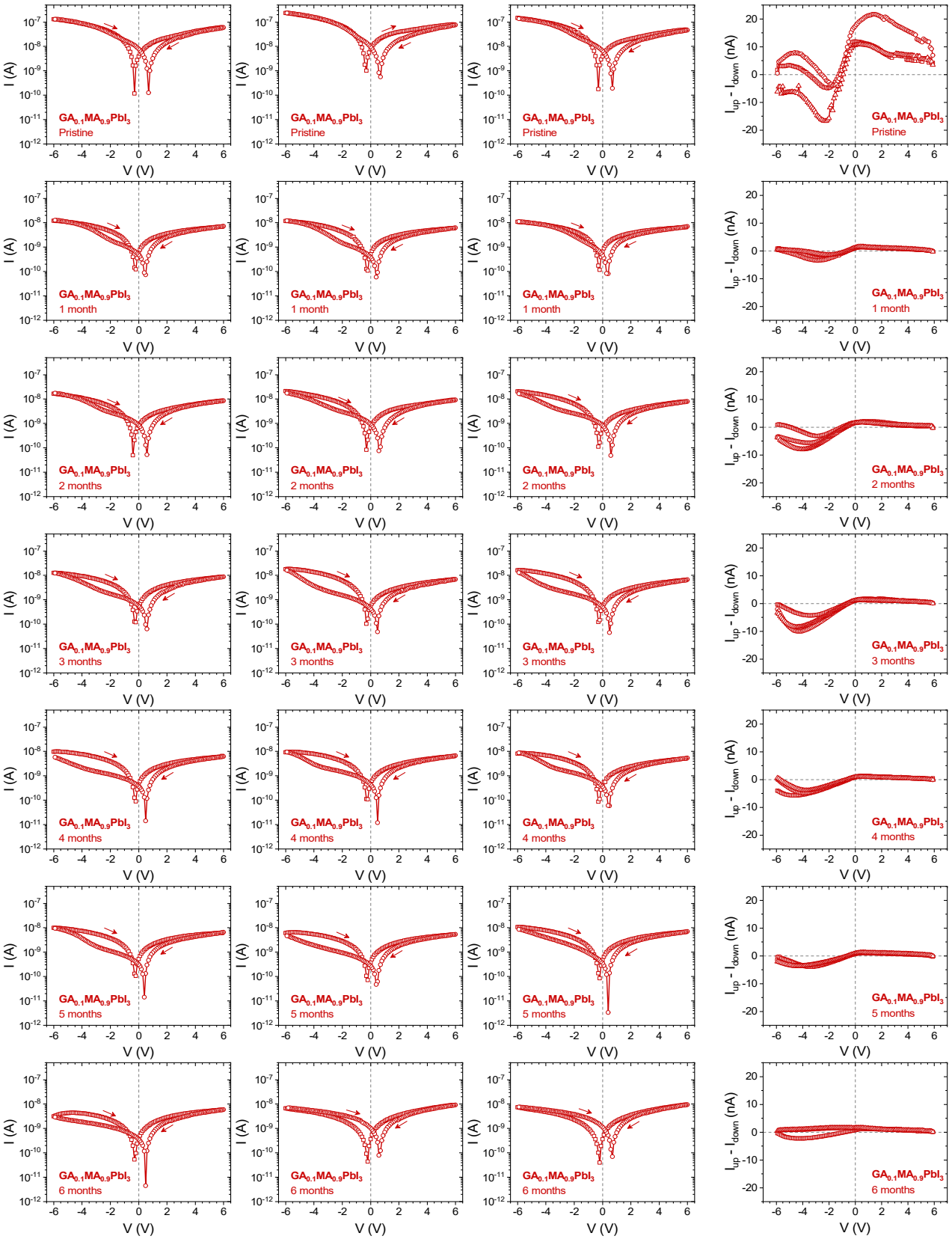

Fig. S10 - Aging evolution of up/down current-voltage curves for $GA_{0.1}MA_{0.9}PbI_3$ on three electrodes. Arrows indicate the direction of measurement. Graphs to the right are the differences between up and down curves at each electrode for a given aging time.

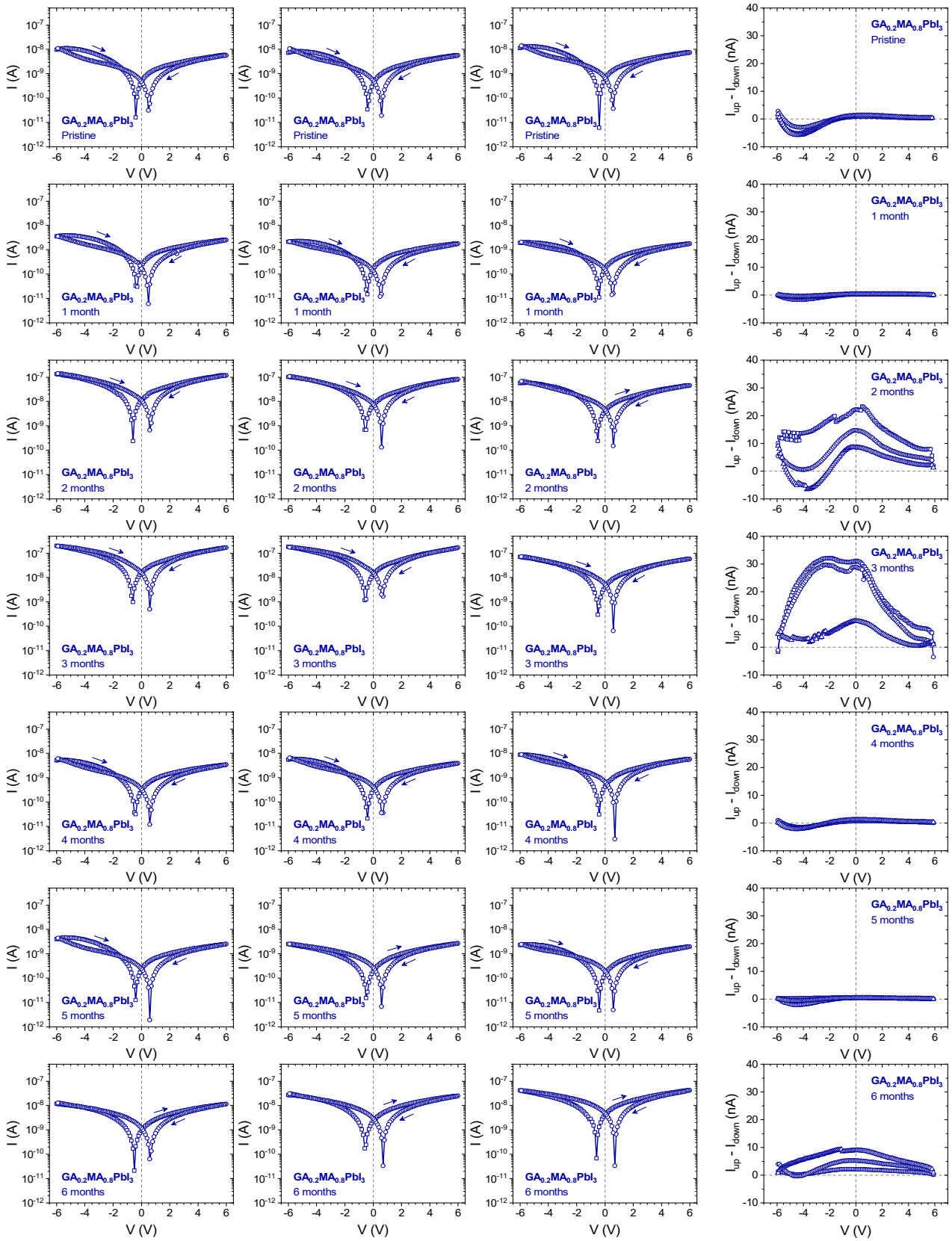

Fig. S11 - Aging evolution of up/down current-voltage curves for $GA_{0.2}MA_{0.8}PbI_3$ on three electrodes. Arrows indicate the direction of measurement. Graphs to the right are the differences between up and down curves at each electrode for a given aging time.

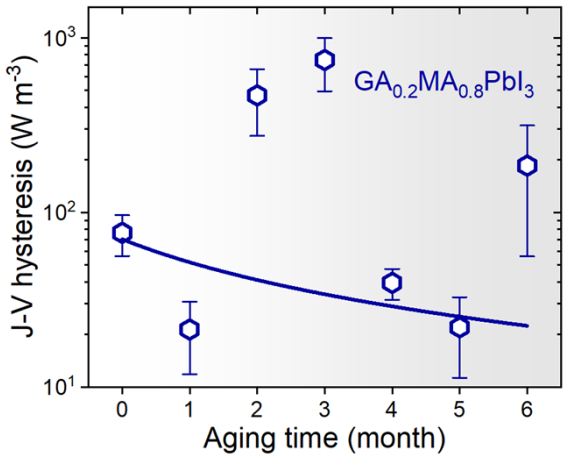

Fig. S12 - J-V hysteresis as a function of the aging time in $GA_{0.2}MA_{0.8}PbI_3$ composition. Error bars are the standard deviation. The line is a merely tentative guide to the eyes. A reduction in the hysteresis with aging was hypothesized based on the discussion on the main text, but cannot be clearly verified.

Supplementary Note 10: Impedance spectroscopy study on pristine and aged $MAPbI_3$

To analyze the temperature-dependent impedance spectroscopy data of pristine and aged $MAPbI_3$, the recorded G and B measurements were treated in terms of complex impedance ($Z^* = Z' - iZ''$) and complex capacitance ($C^* = C' + iC''$). The values of the important components used in this study were calculated using the relations

$$Z' = \frac{G}{B^2 + G^2}$$

$$Z'' = \frac{B}{B^2 + G^2}$$

$$C' = \frac{B}{\omega}$$

where $\omega = 2\pi f$ is the angular frequency. The data were visualized in the form of the Nyquist plots (Z'' vs Z'), and the dispersion of the real component of capacitance, given in Fig. S13.

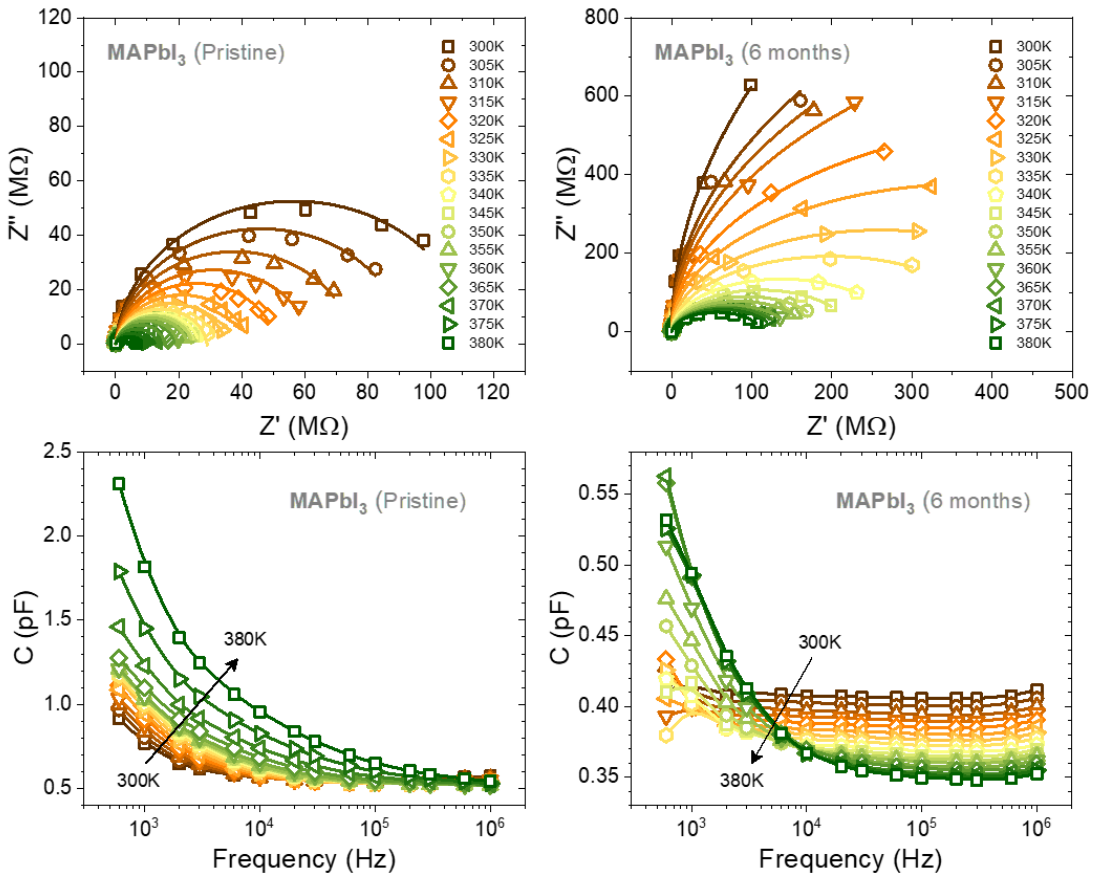

Fig. S13. Nyquist plots (top) and dispersion of real capacitance (bottom) dependency on temperature for pristine and six months-aged $MAPbI_3$. For the Nyquist plots, the lines are fit using the Cole-Cole model. For real capacitance dispersion, the lines are guides for the eyes.

To fit the impedance data, we can use the Cole-Cole relaxation model [6], using the equivalent circuit given in Fig. S14.

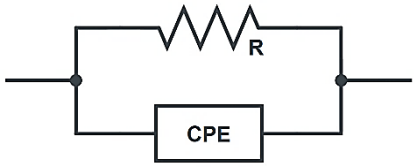

Fig. S14 - Illustration of a possible equivalent circuit representing the Cole-Cole model.

In the Cole-Cole model, it is assumed that the sample might be treated as a parallel association between a resistor of resistance R, and a CPE (constant phase element). In this case, the complex circuit impedance has the form given by:

$$Z^* = \frac{R}{1 + (i\omega\tau)^b}$$

where $\tau = 1/2\pi f_r$ is the mean relaxation time, f_r is the mean relaxation frequency, and b is the Cole-Cole coefficient, an empirical parameter, in the interval between 0 and 1, which reflects the existence of a distribution of relaxation times in the material due to thermal fluctuations, structural inhomogeneities, etc. In this case, the Z'' vs Z' data can be fitted using the following expression as recently applied [2].

$$Z'' = \sqrt{\left[\frac{R}{2}cosec\left(\frac{b\pi}{2}\right)\right]^2 - \left[Z' - \frac{R}{2}\right]^2} - \frac{R}{2}cotg\left(\frac{b\pi}{2}\right)$$

Through an impedance Nyquist plots, the fitting using the above expression provides the values of R and b at a given temperature. Then, considering the equation:

$$\sigma = \frac{d}{aR}$$

where d is the sample thickness (650 μm) and a the electrode area (3.47 x 10^{-7} m²), the dc conductivities (σ) are calculated as a function of temperature. To obtain the dc conductivity activation energies, we modeled the temperature-dependent dc conductivities with an Arrhenius type equation, such that

$$\sigma = \sigma_0 exp\left(\frac{-E_c}{k_B T}\right)$$

where σ_0 is a constant and E_c is the conductivity activation energy. From its linearized form, that is,

$$ln\sigma = ln\sigma_0 - \frac{E_c}{k_B T}$$

we extract the activation energy from the angular coefficient of $ln\sigma$ vs. $1/T$ plots. Finally, the relaxation times (τ) can be calculated using the relation

$\tau = RC$

where C is the sample (geometrical) capacitance. Due to the long frequency plateau, in the case here, C can be approximated by the value of C' at 1 MHz.

Supplementary Note 11: Space-charge limited-current modeling of $MAPbI_3$

General, concise discussions of the SCLC model, and its applications to HPs materials and devices, can be found respectively in [7] and [8]. A sequence of comparative results on HP single crystals using the following equations can be found in [9]. Briefly, for low voltages, it is noticed that the current density varies according to Ohm's law ($J \propto V$), such that

$$J = qn_c\mu\frac{V}{d}$$

where q is the elementary charge (1.602 x 10^{-19} C) , n_c the density of free charge carriers in the dark, μ the charge carrier mobility, and d the distance between the metallic contacts, i.e., the sample thickness. In this conduction regime, the concentration of injected carriers is small compared to the concentration of free carriers in equilibrium with the crystal at a given temperature.

As the voltage increases, the density of injected carriers builds up, and trap states start to be filled. A transition from the ohmic to the so-called trap-filled limit (TFL) occurs, beyond which a typical $J \propto V^n$ ($n > 2$) dependency is observed. This transition occurs at the trap-filled limit voltage (V_{TFL}), such that

$$V_{TFL} = \frac{qn_t d^2}{2\varepsilon'\varepsilon_0}$$

where n_t is the density of traps and, ε' the relative dielectric permittivity and ε the permittivity of free space (8.854 x 10^{-12} F m^{-1}). Using this expression, the density of traps can be calculated from the experimental values of V_{TFL} in the $log\, J$ vs. $log\, V$ graph.

The traps are filled up at sufficiently high voltages, and space charge effects appear. A conduction regime known as the Child's region takes place, which is characterized by the dark currents showing a quadratic dependence with voltage ($J \propto V^2$) according to the famous Mott-Gurney's law,

$$J_D = \frac{9\varepsilon'\varepsilon_0\mu V_D^2}{8d^3}$$

where J_D and V_D are, respectively, the current density and voltage in the Child's region. From this relation, we can calculate the charge carrier mobility, which can then be used to obtain the density of free charge carriers from the conductivity in the ohmic regime (σ_{ohmic}), that is,

$$n_c = \frac{\sigma_{ohmic}}{q\mu}$$

Together, the application of the above relations then allows estimating the variation of n_t, μ and n_c with the aging time. Measurements were set in three electrodes across the sample. The aging evolution of experimental J-V curves for all $GA_xMA_{1-x}PbI_3$ compositions is shown in Fig. S15. The calculated charge carrier parameters for $MAPbI_3$ are given in Table S2.

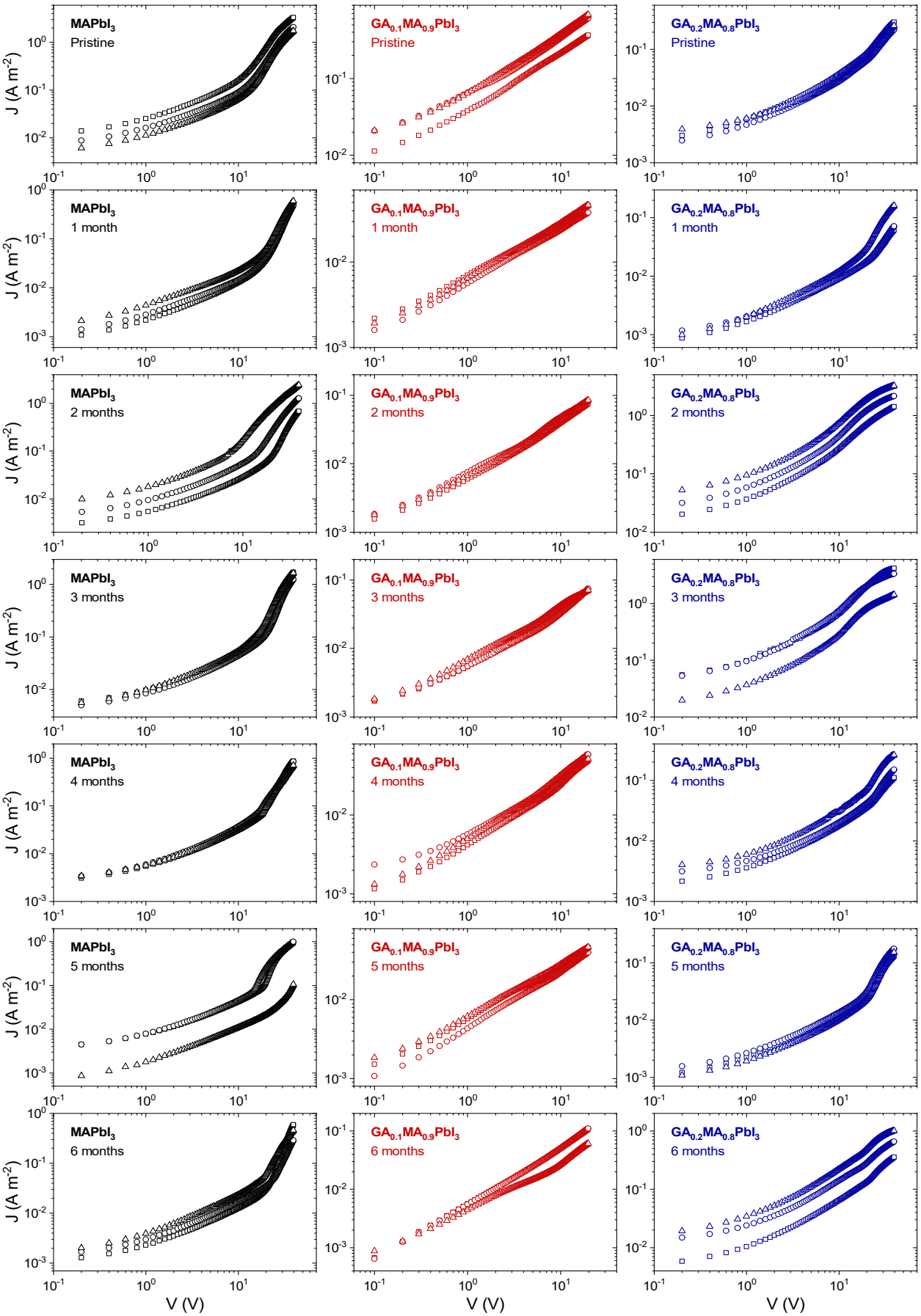

Fig. S15 - Aging evolution of forwarding current density-voltage curves for $GA_xMA_{1-x}PbI_3$ compositions. Each graph shows the measurements on three electrodes.

Table S2 - Experimental data and calculated parameters for $MAPbI_3$ on each aging time. For calculations, we considered d = 650 x 10^{-6} m and ε' = 50. The uncertainties are the standard deviations. *: excluded value.

Aging time (month)	Experimental data			Calculated parameters			
	V_{TFL} (V)	V_D (V)	J_D (A m^{-2})	σ_{ohmic} (10^{-6} S m^{-1})	n_t (10^{17} m^{-3})	μ (10^{-4} m^2 V^{-1} s^{-1})	n_c (10^{16} m^{-3})
0	11.4	28.6	1.92	8.8	1.5	12.9	4.2
	12.0	29.8	1.21	5.0	1.6	7.5	4.1
	12.8	27.0	0.78	3.6	1.7	5.9	3.8
	-	-	-	5.8 ± 2.7	1.6 ± 0.1	8.8 ± 3.7	4.0 ± 0.2
1	17.4	36.0	0.34	0.7	2.3	1.5	3.1
	16.2	36.0	0.36	0.8	2.1	1.5	3.3
	16.4	32.4	0.40	1.2	2.1	2.1	3.5
	-	-	-	0.9 ± 0.2	2.2 ± 0.1	1.7 ± 0.4	3.3 ± 0.2
2	17.0	31.6	0.37	1.6	2.2	2.0	4.8
	12.4	27.2	0.57	3.0	1.6	4.2	4.4
	7.0	18.4	0.68	6.6	0.9	11.1	3.7
	-	-	-	3.7 ± 2.6	1.6 ± 0.7	5.8 ± 4.7	4.3 ± 0.6
3	14.8	29.0	0.78	2.8	1.9	5.1	3.3
	18.0	32.2	0.69	2.5	2.3	3.7	4.2
	14.2	27.0	0.62	3.0	1.8	4.7	4.0
	-	-	-	2.7 ± 0.3	2.0 ± 0.3	4.5 ± 0.8	3.8 ± 0.5
4	17.2	39.0	0.85	1.9	2.2	3.1	3.8
	13.4	39.0	0.82	2.1	1.7	3.0	4.4
	14.4	39.0	0.68	1.8	1.9	2.5	4.5
	-	-	-	1.9 ± 0.2	2.0 ± 0.3	2.8 ± 0.3	4.2 ± 0.4
5	17.6	25.8	0.39	2.5	2.3	3.2	4.8
	13.6	20.8	0.27	2.7	1.8	3.5	4.7
	19.6	39.0	0.10	0.7	2.5	0.4	11.5*
	-	-	-	1.9 ± 1.1	2.2 ± 0.4	2.4 ± 1.7	4.7 ± 0.1
6	19.8	39.0	0.56	0.7	2.6	2.0	2.3
	21.6	39.0	0.27	1.0	2.8	1.0	6.2
	16.6	39.0	0.44	1.4	2.2	1.6	5.4
	-	-	-	1.0 ± 0.3	2.5 ± 0.3	1.5 ± 0.5	4.6 ± 2.1

References

[1] B. Roose et al., *Journal of Physical Chemistry Letters*, 2020, 11, 16, 6505.

[2] F. B. Minussi et al., *Chemical Communications*, 2022, 58, 2212.

[3] T. Roisnel and J. Rodriguez-Carvajal, *Materials Science Forum*, 2001, 118, 378-381.

[4] K. X. Steirer et al., *ACS Energy Letters*, 2016, 1, 2, 360–366.

[5] V. Sarritzu et al., *Advanced Optical Materials*, 2018, 6, 1701254.

[6] K. S. Cole and R. H. Cole., *Journal of Chemical Physics*, 1941, 9, 341.

[7] F.-C. Chiu, *Advances in Materials Science and Engineering*, 2014, 2014, 578168.

[8] J. Peng et al., *Chemical Society Reviews*, 2017, 46, 5714.

[9] W.-G. Li et al., *Journal of Materials Chemistry A*, 2017, 5, 19431-19438.